universe

MDPI

Article

Galactic Core–Tail Structure in BEC Dark Matter with Kapitza Potential

Itauany Barroso [1] and Hermano Velten [2,3,*]

[1] Departamento de Física, Universidade Federal do Espírito Santo (UFES), Campus Goiabeiras, Vitória 29075-910, Brazil; itauany.barroso@edu.ufes.br
[2] Departamento de Física, Universidade Federal de Ouro Preto (UFOP), Campus Morro do Cruzeiro, Ouro Preto 35402-136, Brazil
[3] Instituto de Astronomía Teórica y Experimental, CONICET-UNC, Laprida 854, Córdoba X5000BGR, Argentina
* Correspondence: hermano.velten@ufop.edu.br

Abstract

Recently, the experimental realization of a Kapitza potential in a Bose–Einstein condensate (BEC) was reported for the first time in the literature, motivating further theoretical investigations of such a system. At the same time, in the astrophysical context, BEC dark matter models have been widely studied as a possible phenomenological explanation for the dark matter phenomena. We model the galactic structure with an inner cored profile obtained from the ground state equilibrium solution of the Schrödinger–Poisson together with a Kapitza–BEC-like interaction for the tail region. We find reasonable agreement of the model with representative galaxy rotation curves available in the SPARC catalogue.

Keywords: dark matter; Bose–Einstein condensate; Kapitza pendulum

1. Introduction

The first evidence for dark matter (DM) emerged in 1933, when Fritz Zwicky studied the Coma Cluster and noticed that the visible mass was not sufficient to explain the observed dynamics [1]. Decades later, a different investigation route conducted by Vera Rubin and Kent Ford [2] confirmed this discrepancy, showing that the rotation curves of spiral galaxies remain approximately flat at large radial distances, in contrast with the Keplerian decay expected if only baryonic matter were present. These results paved the idea that dark matter plays a fundamental role in the dynamics and formation of galaxies. Together with several other pieces of evidence from both astrophysical and cosmological contexts, dark matter became a fundamental ingredient in modern astronomy. See Refs. [3–6] for reviews on the dark matter problem.

Widely used density profiles in the literature, such as Navarro–Frenk–White (NFW) [7] and Einasto [8], reproduce the observed behavior at intermediate and large galactocentric radii but present limitations in the central regions. While the NFW model predicts a steeply increasing central density (a cuspy profile), observations of dwarf and low-surface-brightness galaxies suggest the presence of cores with nearly constant density, motivating alternative profiles such as the Burkert model [9]. This discrepancy is known as the cusp–core problem, and it remains a matter of debate in dark matter research [10–12].

In rotation curve analyses, different assumptions regarding the baryonic contribution are commonly adopted. One frequently used limiting case is the minimum disk assumption, in which the observed rotation curve is entirely attributed to the dark matter component. Although this approach is not physically realistic, as it neglects the contribution of the

Check for updates

Academic Editor: Paola Marziani

Received: 26 January 2026
Revised: 19 March 2026
Accepted: 28 March 2026
Published: 31 March 2026

Copyright: © 2026 by the authors. Licensee MDPI, Basel, Switzerland. This article is an open access article distributed under the terms and conditions of the Creative Commons Attribution (CC BY) license.

gaseous disk, which is observationally well established, it provides an upper bound on the allowed concentration of the dark halo. Moreover, it facilitates direct comparison with cosmological simulations, a large fraction of which model only the dark matter component [13]. This assumption, therefore, provides a useful reference framework for assessing the behavior of dark-matter-dominated halo models.

Despite the strong evidence for the existence of a non-luminous component in the Universe, the nature of the dark matter particle remains unknown. Among the many theoretical candidates, an intriguing possibility is that dark matter could be composed of ultralight bosons, such as axions or axion-like particles [14–16]. In this context, the large occupation number of these particles allows the formation of Bose–Einstein condensates (BECs) on astrophysical scales (see, for example, [17–19]). This class of models is often referred to as fuzzy dark matter [20], where the wave nature of ultralight bosons stabilizes central solitonic cores and mitigates the cusp–core discrepancy.

A BEC is a state of matter that arises when a system of bosons occupies the same quantum state at extremely low temperatures [21,22], causing their collective behavior to be described by a single macroscopic wave function [23] and theoretically described by the Gross–Pitaevskii equation [24,25]. In laboratory settings, this phenomenon has been observed in dilute atomic gases cooled to temperatures near absolute zero [26,27]. In an astrophysical context, one can adopt the hypothesis that a similar process could occur naturally if dark matter were composed of ultralight bosonic particles with very small masses $m \sim 10^{-23}$ eV. In this regime, the wave nature of dark matter leads to the emergence of self-gravitating condensates whose dynamics are governed by the Gross–Pitaevskii–Poisson (GPP) system of equations [28,29]. Such models naturally predict core–tail halo structures, in which the central solitonic core is stabilized by quantum pressure, while the outer tail accounts for the approximately flat rotation curves observed at large radius [18,30,31].

Furthermore, as the nature of DM and its possible self-interactions are still unknown, it is conceivable that it may be subject to alternative phenomenological potentials, such as the Kapitza potential. Originally studied in the context of oscillating pendulums, the Kapitza potential produces a dynamic stabilization effect arising from rapid oscillations [32,33]. BEC systems trapped by the Kapitza potential have been recently realized in the laboratory for the first time [34]. Hence, theoretical investigations of such systems are close to the state of the art in this field and, of course, welcomed. In the astrophysical scenario, introducing such a term can significantly modify the system's dynamics, reshaping the density profiles in the tail region and offering a new perspective on halo stability and morphology. This approach also opens the possibility of reproducing the observed rotation curves with greater fidelity.

In this work, we qualitatively investigate the influence of the Kapitza potential parameters, particularly its amplitude, on the shape of rotation curves obtained from the modified GPP system. We treat the Kapitza term as an additional self-interaction, rather than as an arbitrary external trapping potential. Although we cannot yet provide a physical motivation at the microscopic level, it modifies the internal dynamics in the tail region of the condensate rather than acting as an externally imposed background. Our goal is precisely to isolate and understand how this specific dynamical mechanism alters the tail behavior, the core–tail transition, and the resulting rotation curves in case it can be applied to the galactic structure. Our goal is to understand how variations in this parameter affect the halo stability, the transition radius between the core and tail, and the behavior of the orbital velocities. Apart from emphasizing a qualitative analysis aimed at revealing the physical role of the Kapitza potential in shaping galactic dynamics, we also employ a quantitative fitting with representative available data from the SPARC catalogue [35]. For comparison purposes, we also confront the resulting total rotation curves with those

obtained from standard density profiles widely used in the literature considering the full galactic rotation curve. We conduct our analysis within the non-relativistic framework which is well justified at the galactic scale.

This paper is organized as follows: In the next section we present the model for the galactic structure and outline the governing equations. Section 3 introduces the density profiles employed for comparison in the analysis, namely, the NFW, Einasto, and Burkert models. Section 4 presents the results, including the rotation curve fits, the corresponding density profiles, and an analysis of the influence of the interaction parameter ϵ and the Kapitza potential amplitude $V_{0\mathrm{Kap}}$. This section also includes a subsection with the best-fitting parameters and the chi-square values. In Section 5, we provide a detailed discussion of the implications of our findings. Finally, Section 6 summarizes our conclusions.

2. The Model

To describe our model, we start by following the approach proposed in [31]. Modeling dark matter as a Bose–Einstein condensate requires the use of two equations. The first is the Gross–Pitaevskii (GP) equation, a non-linear variant of the time-dependent Schrödinger equation that governs the temporal evolution of the macroscopic wave function of the condensate. This equation is employed because it effectively accounts for the interactions between identical particles in the condensate. In its extended version, which includes further self-interaction terms $g'(|\psi|^2)$, it is given by

$$i\hbar\partial_t\psi = -\frac{\hbar^2}{2m}\nabla^2\psi + \frac{4\pi\hbar^2}{m}a_s|\psi|^2\psi + g'(|\psi|^2)\psi + V\psi, \tag{1}$$

where $\hbar$ is the reduced Planck constant, t is the temporal coordinate, m is the atomic mass, a_s is the scattering length between atoms ($a_s > 0$ for repulsive interactions, $a_s < 0$ for attractive interactions) and $|\psi|^2$ represents the particle density of the condensate. The total interaction is given by the gravitational potential V, which obeys the Poisson equation

$$\nabla^2 V = 4\pi G|\psi|^2, \tag{2}$$

and, therefore, characterizes the self-gravitating nature of such an object, where G is the gravitational constant, and by the phenomenological self-interacting trapping potential V_{Kap} of the Kapitza type:

$$g'(|\psi|^2) = V_{0\mathrm{Kap}}\exp\left(-\frac{2r^2}{a^2}\right)\cos(\omega t + \phi_0)|\psi|^2. \tag{3}$$

The parameters a and $V_{0\mathrm{Kap}}$ are the waist and amplitude of the Gaussian profile, respectively, ω is the frequency and ϕ_0 is the phase term of the oscillation.

Similar attempts to extend the standard GPP systems have been performed in the literature, e.g., including non-linear interactions of the cubic and logarithmic type [36,37], as done in Refs. [37–39]. Apart from the aforementioned references, it is worth noting that the logarithmic correction has also been successfully employed in addressing the so-called sound propagation puzzle in dilute BECs [40]. In general, with this kind of extended approach for the non-linearities, one is able to provide a richer phenomenology of this class of models. Again, as stated before, a possible interpretation of the present model is that one can phenomenologically describe the condensate self-interaction based on the trapping mechanism provided by the Kapitza potential.

2.1. Madelung's Transformation

In order to reformulate the Gross–Pitaevskii equation in a hydrodynamic framework, we apply the Madelung transformation by writing the condensate wave function as $\psi = \sqrt{\rho}e^{iS}$, where ρ is the mass density and S is the phase of the wave function. This transformation enables us to describe the system using two real variables, ρ and S, and interpret its dynamics within the quantum hydrodynamic formalism. Readers not familiar with the Madelung transformation and its physical interpretation may consult Refs. [41,42]. Substituting this expression into the Gross–Pitaevskii and Poisson equations and separating the real and imaginary parts, we obtain the following set of equations.

The real part of the Gross–Pitaevskii equation reads

$$\hbar\partial_t S + Q + \frac{\hbar^2}{2m}|\vec{v}|^2 + \frac{4\pi\hbar^2 a_s}{m}\rho + V + V_{0\mathrm{Kap}}\exp\left(-\frac{2r^2}{a^2}\right)\cos(\omega t + \phi_0)\rho = 0, \tag{4}$$

the imaginary part yields the continuity equation

$$\hbar\partial_t\rho + \frac{\hbar^2}{m}[\nabla\cdot(\rho\vec{v})] = 0, \tag{5}$$

and the Poisson equation becomes

$$\nabla^2 V = 4\pi G\rho. \tag{6}$$

Here, $\vec{v} := \nabla S$ represents the velocity field of the quantum fluid. The definition

$$Q = -\frac{\hbar^2}{2m}\frac{\nabla^2\sqrt{\rho}}{\sqrt{\rho}} \tag{7}$$

represents the quantum potential, and V is the gravitational potential generated by the mass density ρ. This hydrodynamic formulation is widely adopted in the literature because it highlights the analogy between a self-gravitating condensate and a compressible fluid with an additional quantum pressure term. For convenience, the notation can be simplified by adopting natural units, $\hbar = m = 4\pi G = 1$ and we define $\epsilon = 4\pi a_s$. Assuming spherical symmetry and a stationary density profile, we take the ansatz for the phase

$$S(t, r) = -V_0 t + \overline{S}(r), \tag{8}$$

where r is the radial coordinate. As we seek stationary solutions, the Kapitza potential is treated as time independent by setting $t = 0$ and $\phi_0 = 0$, so that only its radial dependence enters the equations. This assumption allows us to isolate the static influence of the Kapitza term on the tail structure. Under the assumptions of stationarity and spherical symmetry, the Gross–Pitaevskii–Poisson system reduces to three coupled ordinary differential equations:

$$Q + \frac{1}{2}v^2 + \epsilon\rho + V + V_{0\mathrm{Kap}}\exp\left(-\frac{2r^2}{a^2}\right)\rho = V_0, \tag{9}$$

$$\frac{1}{r^2}\frac{d}{dr}(r^2\rho v) = 0, \tag{10}$$

$$\frac{1}{r^2}\frac{d}{dr}\left(r^2\frac{dV}{dr}\right) = \rho, \tag{11}$$

where the radial velocity is $v := \frac{d\overline{S}}{dr}$.

2.2. Core and Tail Structure

In order to construct a consistent description of the dark matter halo, we adopt a core–tail decomposition, in which the system is divided into two radial regions separated by a transition radius r_t. The inner region, referred to as the core, corresponds to $r < r_t$ and is characterized by a solitonic configuration, while the outer region, referred to as the tail, corresponds to $r \geq r_t$ and is described by the stationary solution of the Gross–Pitaevskii–Poisson system.

Solving the system (9)–(11), we find

$$\rho'_{\text{tail}} = u_{\text{tail}}, \tag{12}$$

$$u'_{\text{tail}} = 4\left[\frac{1}{2}v^2_{\text{tail}} + V_{\text{tail}} - V_0\right]\rho_{\text{tail}} + 4V_{0\text{Kap}}\exp\left(-\frac{2r^2}{a^2}\right)\rho^2_{\text{tail}} - \frac{2u_{\text{tail}}}{r} + \frac{u^2_{\text{tail}}}{2\rho_{\text{tail}}} + 4\epsilon\rho^2_{\text{tail}}, \tag{13}$$

$$V'_{\text{tail}}(r) = \frac{M_{\text{tail}}(r)}{r^2}, \tag{14}$$

$$M'_{\text{tail}}(r) = r^2\rho_{\text{tail}}(r), \tag{15}$$

$$\overline{S}'_{\text{tail}}(r) = v_{\text{tail}}(r), \tag{16}$$

where V_0 is constant, $' := \frac{d}{dr}$, and $v_{\text{tail}} = \frac{A}{r^2\rho_{\text{tail}}}$ is the velocity in the tail region, with A constant, playing, therefore, the role of the system's dynamical constraint. In the absence of self-interactions and of the Kapitza potential, i.e., for $\epsilon = 0$ and $V_{0\text{Kap}} = 0$, the equations obtained here reduce to those in Ref. [31], which provides the reference framework upon which the present model is built.

In the innermost region of the halo, the density profile is dominated by a solitonic structure corresponding to the ground state equilibrium solution of the Gross–Pitaevskii–Poisson system. In the non-interacting limit, this system reduces to the Schrödinger–Poisson equations solved in Refs. [18,30]. Using fully cosmological, high-resolution three-dimensional simulations, the authors of the latter references showed that every virialized halo hosts a central, gravitationally self-bound solitonic core. By fitting the numerically obtained soliton solutions, an accurate analytical approximation for the core density profile was derived, valid within a few core radii. The resulting core density profile is given by

$$\rho_{\text{core}}(r) = \rho_{0\text{core}}\left[1 + 0.091\left(\frac{r}{r_c}\right)^2\right]^{-8}, \tag{17}$$

where $\rho_{0\text{core}}$ is the central density and r_c is the characteristic core radius.

As the radial derivative of the density is defined as $u_{\text{core}} = \rho'_{\text{core}}$, we obtain

$$u_{\text{core}}(r) = -\frac{1.456\, r\, \rho_{0\text{core}}}{\left(1 + \frac{0.091r^2}{r_c^2}\right)^9 r_c^2}. \tag{18}$$

For the core region ($r < r_t$), the total mass enclosed within radius r is given by

$$M_{\text{core}}(r) = 4\pi\int_0^r \rho_{\text{core}}(r')\, r'^2\, dr', \tag{19}$$

and the corresponding gravitational potential must include the contribution from both the inner mass and the outer shells of the density distribution. Assuming that the core solution is valid up to the transition radius r_t, the potential can be written as

$$V_{\rm core}(r) = -\frac{4\pi G}{r}\int_0^r \rho_{\rm core}(r')\, r'^2\, dr' - 4\pi G \int_r^{r_t} \rho_{\rm core}(r')\, r'\, dr'. \tag{20}$$

As in the tail region, we work in rescaled units in which the multiplicative constants can be absorbed into the definition of the variables. Therefore, in the numerical implementation, the factors $4\pi G$ are omitted without loss of generality.

The central structure, being spherically symmetrical and dynamically stable, represents the region of the halo sustained by quantum pressure. It transitions smoothly into the outer tail, where the density decreases gradually and the classical regime becomes dominant.

The profile provided by (20) is valid only for the inner region $r < r_t$. Beyond this, the tail profile calculated numerically from the set (12)–(16) is adopted. To ensure continuity between the core and the tail, we impose the following boundary conditions:

$$\begin{aligned} \rho_{\rm tail}(r_t) &= \rho_{\rm core}(r_t); \\ u_{\rm tail}(r_t) &= u_{\rm core}(r_t); \\ V_{\rm tail}(r_t) &= V_{\rm core}(r_t); \\ M_{\rm tail}(r_t) &= M_{\rm core}(r_t). \end{aligned}$$

3. Dark Matter Density Profiles

In this section, we present the dark matter density profiles widely used in the literature that will be used as reference models for comparison with the results obtained from the model developed in this paper.

3.1. Navarro–Frenk–White (NFW) Profile

The NFW density profile [7] is defined by

$$\rho_{\rm NFW}(r) = \frac{\rho_s}{\left(\frac{r}{r_s}\right)\left(1+\frac{r}{r_s}\right)^2}, \tag{21}$$

where ρ_s is a characteristic density and r_s is the scale radius.

The enclosed mass has an analytical solution:

$$M_{\rm NFW}(r) = 4\pi\rho_s r_s^3\left[\ln(1+x) - \frac{x}{1+x}\right], \qquad x = \frac{r}{r_s}. \tag{22}$$

3.2. Einasto Profile

The Einasto density profile was defined in the paper [8]. In this work, we adopt the approach [43], where

$$\rho_{\rm Ein}(r) = \rho_{-2}\,\exp\left[-\frac{2}{\alpha}\left(\left(\frac{r}{r_{-2}}\right)^{\alpha} - 1\right)\right]. \tag{23}$$

Here, ρ_{-2} and r_{-2} are the density and radius at which the logarithmic slope of the density profile is equal to -2, i.e., $d\ln\rho/d\ln r|_{r=r_{-2}} = -2$. For details on other conventions and their corresponding conversions, see [44].

The enclosed mass is given by $M_{\rm Ein}(r) = 4\pi\int_0^r \rho_{\rm Ein}(r')\, r'^2\, dr'$.

3.3. Burkert Profile

The Burkert density profile [9] is defined as

$$\rho_{\mathrm{Bur}}(r) = \frac{\rho_0}{\left(1+\frac{r}{r_0}\right)\left[1+\left(\frac{r}{r_0}\right)^2\right]}, \tag{24}$$

where ρ_0 is the central density and r_0 is the scale radius.

The enclosed mass has an analytical form given by

$$M_{\mathrm{Bur}}(r) = \pi\rho_0 r_0^3\Big[\ln(1+x^2) + 2\ln(1+x) - 2\arctan(x)\Big], \qquad x = \frac{r}{r_0}. \tag{25}$$

4. Results

To adjust our model with observational data, transforming the system into physical units, we use scaling factors for time and mass, respectively,

$$t_S = \frac{m r_S^2}{\hbar}, \quad M_S = \frac{\hbar^2}{4\pi G m^2 r_S}. \tag{26}$$

The scale factors are defined from r_S, which represents a specific length chosen according to Ref. [31]. From these quantities, other scaling factors can be defined, such as the density scale $\rho_S = M_S/r_S^3$ and the velocity scale $v_S = r_S/t_S$.

To work with typical galaxy scales, let us consider a reference wavelength $r_S = 1.714$ kpc and an ultra-light boson mass $m = 10^{-23}\,\mathrm{eV/c^2}$. From these values, the scaling factors for time and mass are given by $t_S = 14.97$ My and $M_S = \frac{5}{4\pi} \times 10^9$ M$\odot$. Furthermore, the scale factors associated with density and velocity are $\rho_S = 7.901 \times 10^7$ M$\odot$/kpc^3 and $v_S = 112.0$ km/s, respectively. Thus, to obtain the rotation curves and density profiles of our model in physical units, we multiply the scaling factors v_S and ρ_S in the final expressions for velocity and density, respectively.

4.1. Rotation Curves and Density Profiles

To plot the rotation curves (RC) for all density models considered in this work, we adopt the general expression

$$v_{\mathrm{RC}}(r) = \sqrt{\frac{GM(r)}{r}}, \tag{27}$$

where $M(r)$ is the enclosed mass associated with the corresponding density profile, whether defined analytically (NFW, Einasto, Burkert, solitonic core) or obtained numerically from the system in the tail region. We have, therefore, a kind of hybrid model, both analytical for the solitonic core and numerical for the tail.

Figures 1 and 2 present the rotation curves (left panels) resulting from the corresponding density profiles (right panels) for the galaxies NGC 2903, NGC 3198, UGC 11914, ESO 563-G021, NGC 2366, NGC 2403 and UGC 08490. In the left panels, one can also visualize the observational data with the fits obtained by the different models tested. The adopted parameters values are shown later in Table 1. Within the adopted minimum disk approach, each classical profile (NFW, Einasto, and Burkert) is contrasted with the model proposed in this work, composed of a solitonic core and a dynamic tail region. The transition radius r_t, which delimits the interface between the core and tail, is indicated by a vertical dashed line in all panels. The rotation curves show the predicted behavior for the circular velocity $V_{RC}(r)$, while the log–log plots display the radial density drop for each profile.

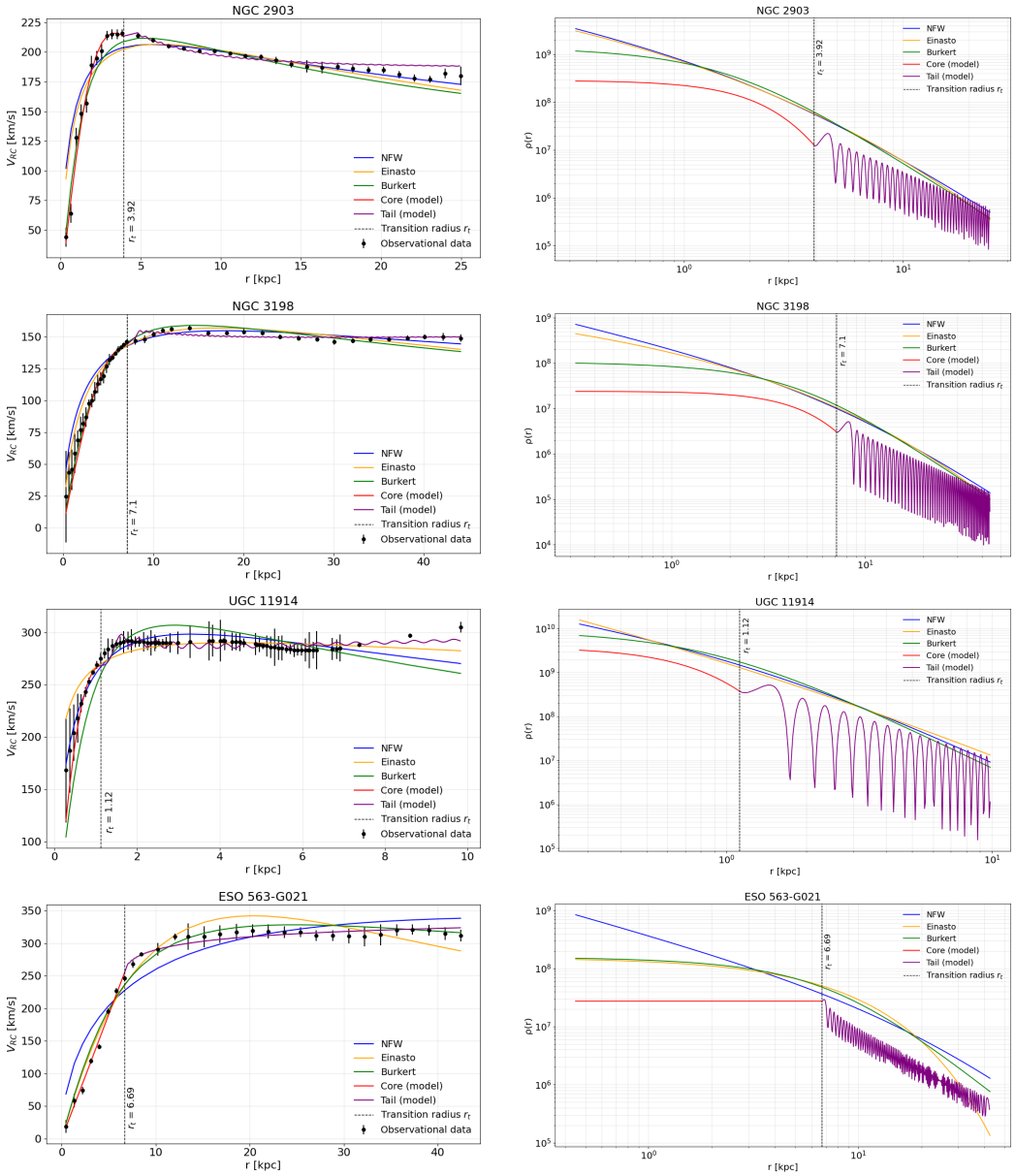


Figure 1. Rotation curves (**left panels**) and density profiles in log–log scale (**right panels**) for the galaxies analyzed. The NFW, Einasto, Burkert profiles and the solitonic core–tail model are shown. The dashed line indicates the transition radius r_t. The adjusted parameters are listed in Table 1.

Table 1. Best-fitting parameters of the profiles. Fixed parameters: $\epsilon = 1$, $a = r_t$.

Galaxy	Model	Parameters Adjusted	χ^2	$\chi^2_{v_Total}$
NGC 2903	Our model	$\rho_{0\text{core}} = 3.63148$, $r_c = 1.71602$, $A = 10.7143$, $V_0 = 21.1224$, $V_{0\text{Kap}} = 994.9495$	79.7784	4.76259
NGC 2903	NFW	$\rho_s = 5.397 \cdot 10^8$, $r_s = 2.60$	248.318	23.0119
NGC 2903	Einasto	$\rho_{-2} = 1.069 \cdot 10^8$, $r_{-2} = 2.93$, $\alpha = 0.258$	268.458	25.4917
NGC 2903	Burkert	$\rho_0 = 1.472 \cdot 10^9$, $r_0 = 1.62$	175.458	11.279
NGC 3198	Our model	$\rho_{0\text{core}} = 0.30623$, $r_c = 3.95455$, $A = 4.0816$, $V_0 = 13.0612$, $V_{0\text{Kap}} = 2787.5510$	50.149	2.69309
NGC 3198	NFW	$\rho_s = 3.006 \cdot 10^7$, $r_s = 8.26$	145.242	7.36916
NGC 3198	Einasto	$\rho_{-2} = 7.63 \cdot 10^6$, $r_{-2} = 8.42$, $\alpha = 0.317$	129.295	7.00375
NGC 3198	Burkert	$\rho_0 = 1.084 \cdot 10^8$, $r_0 = 4.48$	104.409	5.47683

Table 1. *Cont.*

Galaxy	Model	Parameters Adjusted	χ^2	$\chi^2_{\nu_Total}$
UGC 11914	Our model	$\rho_{0\text{core}} = 48.47837$, $r_c = 0.58303$, $A = 9.6970$, $V_0 = 29.6970$, $V_{0\text{Kap}} = 82.8283$	55.7716	1.46824
UGC 11914	NFW	$\rho_s = 3.254 \cdot 10^9$, $r_s = 1.53$	254.756	5.76105
UGC 11914	Einasto	$\rho_{-2} = 4.927 \cdot 10^8$, $r_{-2} = 1.84$, $\alpha = 0.09$	147.617	6.43989
UGC 11914	Burkert	$\rho_0 = 1 \cdot 10^{10}$, $r_0 = 0.90$	686.048	36.318
ESO 563-G021	Our model	$\rho_{0\text{core}} = 0.34854$, $r_c = 70{,}439.62462$, $A = 92.8571$, $V_0 = 69.3878$, $V_{0\text{Kap}} = 1267.3469$	40.0484	4.94875
ESO 563-G021	NFW	$\rho_s = 1.559 \cdot 10^7$, $r_s = 25.22$	811.634	115.631
ESO 563-G021	Einasto	$\rho_{-2} = 2.087 \cdot 10^7$, $r_{-2} = 12.03$, $\alpha = 1$	198.959	28.3002
ESO 563-G021	Burkert	$\rho_0 = 1.601 \cdot 10^8$, $r_0 = 7.61$	192.979	27.7411
NGC 2366	Our model	$\rho_{0\text{core}} = 0.14003$, $r_c = 2.06459$, $A = 2.1212$, $V_0 = 25.2525$, $V_{0\text{Kap}} = 60.6061$	13.2729	1.22728
NGC 2366	NFW	$\rho_s = 1.045 \cdot 10^6$, $r_s = 27.37$	110.4	10.41
NGC 2366	Einasto	$\rho_{-2} = 7.366 \cdot 10^6$, $r_{-2} = 3.12$, $\alpha = 1$	13.1045	1.34651
NGC 2366	Burkert	$\rho_0 = 5.41486 \cdot 10^7$, $r_0 = 2.08978$	21.6403	1.99493
NGC 2403	Our model	$\rho_{0\text{core}} = 4.15658$, $r_c = 0.56607$ $A = 2.6263$, $V_0 = 4.5455$, $V_{0\text{Kap}} = 26.2626$	724.227	12.6455
NGC 2403	NFW	$\rho_s = 4.444 \cdot 10^7$, $r_s = 5.70$	615.187	17.4867
NGC 2403	Einasto	$\rho_{-2} = 9.122 \cdot 10^6$, $r_{-2} = 6.27$, $\alpha = 0.217$	587.506	15.4888
NGC 2403	Burkert	$\rho_0 = 2.943 \cdot 10^8$, $r_0 = 2.21$	4918.37	300.986
UGC 08490	Our model	$\rho_{0\text{core}} = 3.19368$, $r_c = 0.492455$, $A = 3.4343$, $V_0 = 28.1818$, $V_{0\text{Kap}} = 32.3232$	26.5759	3.57014
UGC 08490	NFW	$\rho_s = 8.65038 \cdot 10^7$, $r_s = 2.51758$	3.54876	1.63572
UGC 08490	Einasto	$\rho_{-2} = 2.255 \cdot 10^7$, $r_{-2} = 2.49$, $\alpha = 0.280$	2.79813	0.649813
UGC 08490	Burkert	$\rho_0 = 4.31961 \cdot 10^8$, $r_0 = 1.16206$	24.9981	12.863

Previous studies (e.g., [31,45]) typically find the transition between the solitonic core and the outer halo at approximately $r_t \sim 3.5 r_c$. However, in the present work, we adopt r_c as a free model parameter to be adjusted with the data while r_t is treated as an arbitrary parameter used to match the inner solitonic core solution to the outer tail solution in an arbitrary way. We tested the model with different values of r_t, and although these values are not derived from first principles, the adopted range provides numerically stable solutions and acceptable fits to the observed rotation curves. As the core density profile is described by a form with free parameters $\rho_{0\text{core}}$ and r_c, determined independently for each galaxy, enforcing a fixed proportionality between r_t and r_c would assume a universal core scale, which is not physically justified. Therefore, r_t is introduced as an effective matching scale representing the transition between the core-dominated and halo-dominated regimes.

4.2. Fitting Analysis

To adjust the NFW, Einasto, Burkert, and soliton core density profiles, we used the non-linear least squares method implemented in Python 3.12.0 through the curve_fit algorithm from the scipy.optimize module [46]. For the tail region, which is described by a dynamical model derived from a system of coupled differential equations, a different strategy was adopted. Instead of a direct functional fit, the tail solution was obtained through numerical integration of the system for each combination of the free parameters A, V_0 and $V_{0\text{Kap}}$. For a given parameter set, the resulting rotation curve was evaluated at the same radii as the observational data, and the quality of the fit was quantified using the chi-square statistic.

The optimal parameters were identified through a systematic exploration of the parameter space, seeking solutions that minimize chi-square statistics, which are described below.

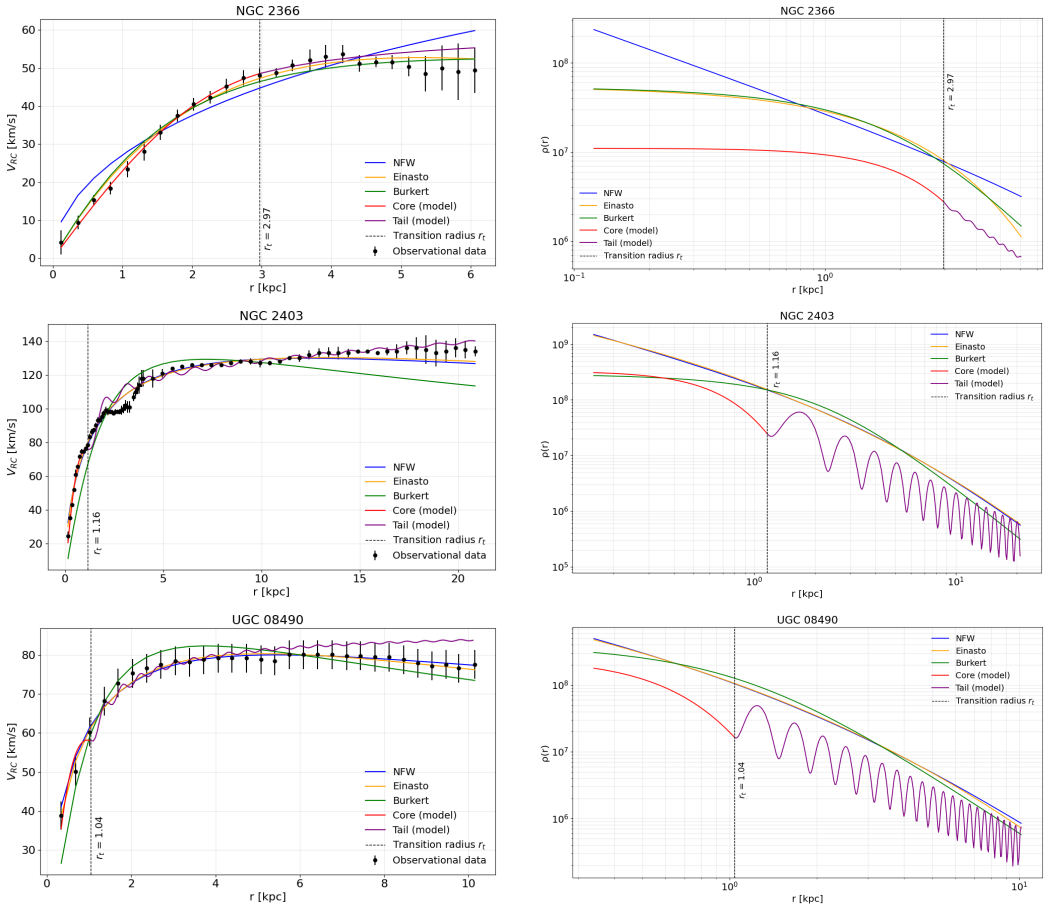


Figure 2. The same as Figure 1 for different galaxies.

The chi-square method (χ^2) allows us to quantify the deviation between the values predicted by the model and the observed velocities, weighting each discrepancy by the experimental uncertainties associated with each data point (books such as [47] offer in-depth explanations of the method). Explicitly, the chi-square is defined by

$$\chi^2 = \sum_{i=1}^{N} \frac{[v_{\rm obs}(r_i) - v_{\rm mod}(r_i)]^2}{\sigma_i^2}, \tag{28}$$

where $v_{\rm obs}(r_i)$ is the observational velocity at radius r_i, $v_{\rm mod}(r_i)$ is the velocity calculated by the model at the same point, and σ_i represents the error associated with the experimental measurement. Thus, smaller values of χ^2 correspond to models that provide a closer fit to the observed rotation curves.

Although the absolute value of χ^2 is informative, we use the reduced chi-square test to determine the adjusted core and tail parameters, as this metric normalizes the error by the number of degrees of freedom and allows us to reliably identify which parameter combinations produce statistically consistent fits. The reduced chi-square is defined as

$$\chi^2_\nu = \frac{\chi^2}{N - p}, \tag{29}$$

where N is the number of observational points and p is the number of adjusted parameters. This procedure normalizes the chi-square by the number of degrees of freedom, ν =

$N - p$, allowing for consistent statistical interpretation. Values of $\chi^2_\nu \approx 1$ indicate that the model adequately reproduces the observed velocities within the experimental uncertainties; much higher values suggest physical inadequacy or unconsidered systematic errors, while much lower values may indicate overfitting or underestimation of uncertainties. In our model, however, the core and the tail descriptions have a different number of free model parameters. We calculate the total reduced chi-square statistics as the sum of the two (core+tail) components. We then compute $\chi^2_{\nu_core}$ and $\chi^2_{\nu_tail}$ and adopt

$$\chi^2_{\nu_Total} = \frac{\chi^2_{core}}{N_{core} - p_{core}} + \frac{\chi^2_{tail}}{N_{tail} - p_{tail}}. \tag{30}$$

As we are adding the reduced chi-square for two different regions, we should expect now that values ≈ 2 indicate a good agreement with data.

Table 1 presents the adjustments obtained for the different density profiles applied to the analyzed galaxies. In order to reduce the dimensionality of the parameter space and make the fitting procedure computationally feasible, we adopted physically motivated priors for some model parameters. In particular, we fixed $\epsilon = 1$ and set $a = r_t$ in all fits. These parameters can be fixed because ϵ is related to the ratio between the scattering length and the dark matter particle mass, while the a measures the spatial scale of the Kapitza-like interaction. This choice allows us to isolate the dynamical impact of the tail parameters while keeping the number of free parameters manageable. We could also fix $V_{0\mathrm{Kap}}$, but this parameter was intentionally left free in order to test in which galaxies the Kapitza-like interaction may play a relevant dynamical role. For each object, the adjusted parameters of the model proposed in this work are listed, as well as the characteristic parameters of the NFW, Einasto, and Burkert profiles. The table also shows the respective chi-square values χ^2, as well as the reduced one $\chi^2_{\nu_Total}$, allowing comparison of the performance of each model in reproducing the observed rotation curves.

5. Discussions

In Figures 1 and 2, we compare the radial velocity profile of the Kapitza core–tail model developed in this work with observational data and with classical profiles widely used in the literature, simultaneously analyzing the rotation curves and density profiles.

In Figure 1, we group the galaxies for which the proposed model provides the best performance in fitting the rotation curves, based on the χ^2 values presented in Table 1. The galaxies NGC 2903 and NGC 3198 are classified as barred spiral galaxies, while UGC 11914 and ESO 563-G021 are spiral galaxies. For this set of objects, the core–tail model outperforms the other density profiles considered.

In Figure 2, we group the galaxies for which the fit obtained with the proposed model is not the best among all profiles, but still remains competitive. For the irregular galaxy NGC 2366, the proposed model yields a fit comparable to the Einasto profile and superior to the NFW profile; however, the Burkert profile provides the best overall fit. In the case of NGC 2403, a spiral galaxy, although the χ^2 value associated with the proposed model is larger than those of the NFW and Einasto profiles, its $\chi^2_{\nu\text{-Total}}$ is smaller, indicating a better overall agreement with the data when accounting for the number of degrees of freedom. Finally, for the spiral galaxy UGC 08490, although the $\chi^2_{\nu\text{-Total}}$ values of the NFW and Einasto profiles are below 2, they remain closer to this reference value than that obtained with the proposed model. Thus, in this case, the proposed model only outperforms the Burkert profile. Basic properties and morphological classifications of the galaxies were obtained from the NASA/IPAC Extragalactic Database (NED) [48].

Furthermore, in the inner region, the resulting density profiles exhibit cored behavior, consistent with the soliton solution expected for dark matter condensates. This result

agrees with models based on the Schrödinger–Poisson equations, frequently cited as potential alternatives to solve the cusp–core problem, as they provide halo centers with approximately constant density.

We also find that the numerical solutions exhibited oscillations in the tail region, whose amplitude is associated with the values assigned to the parameters A and V_0. These unexpected oscillations are independent of the Kapitza potential and were already found in Refs. [31,49]. To the best of our knowledge, their physical origin is not explicitly discussed in the existing literature. This fact suggests that the mathematical structure of the tail's system may induce intrinsic oscillatory regimes, whose physical interpretation still requires further investigation.

In Figure 3, we show the rotation curves of the galaxy NGC 2903, highlighting the contribution of the solitonic core and the behavior of the tail region for different values of the interaction parameter ϵ in the left panel and $V_{0\mathrm{Kap}}$ in the right panel. It clearly shows how the tail solution of the core–tail model responds to variations in the BEC parameter ϵ (left panel) and in the Kapitza potential magnitude parameter $V_{0\mathrm{Kap}}$ (right panel). In the left panel, different values of the self-interaction parameter ϵ directly alter the effective lift of the halo in the outer region. We saw that positive values increase the orbital velocity after the transition radius r_t, producing a more sustained curve, while negative values reduce this lift and lead to a steeper decline. In the right panel, a qualitatively similar response is observed when varying the amplitude of the Kapitza potential $V_{0\mathrm{Kap}}$. Increasing $V_{0\mathrm{Kap}}$ results in a more sustained tail with higher rotational velocities, while smaller values lead to a decrease. This confirms that the Kapitza potential provides an additional mechanism for regulating the halo dynamics in the tail region.

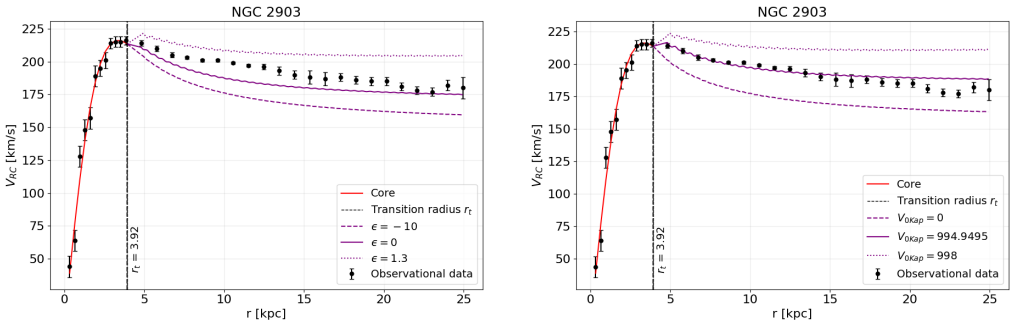


Figure 3. Rotation curve of the galaxy NGC 2903 fitted by the core–tail model. The part $r < r_t$ corresponds to the solitonic core, while $r \geq r_t$ corresponds to the numerical tail solution, shown for different values of ϵ in the left panel and for different values of $V_{0\mathrm{Kap}}$ in the right panel. The dashed vertical line indicates the transition radius r_t. In both panels, the remaining reference values for the parameters are those presented in Table 1. In each isolated variation, whether of ϵ or $V_{0\mathrm{Kap}}$, all other parameters remain fixed at the values in the table.

We also observe a non-linear sensitivity of the model with respect to both ϵ and $V_{0\mathrm{Kap}}$. For values below the adopted parameters (e.g., $\epsilon = -10$ or $V_{0\mathrm{Kap}} = 0$), the rotation curve decreases in a relatively smooth and controlled manner. However, for values above these reference values (e.g., $\epsilon > 1$ or $V_{0\mathrm{Kap}} > 994.9495$), even small increments lead to a significant increase in the rotation curve. As a result, exploring this parameter region requires a more careful and gradual variation, highlighting the strong non-linear response of the model in this regime.

Therefore, from the results presented in Table 1, we found that the model shows competitive performance in relation to the NFW, Einasto, and Burkert profiles. In several galaxies, the fit was elaborate or even superior to these empirical models, establishing that

the combination of a solitonic core and a dynamic tail constitutes a consistent description for galactic halos.

6. Conclusions

This paper was based on a theoretical study of dark matter halos modeled as Bose–Einstein condensates, which are subject to an extra Kapitza-type potential, as recently realized in the laboratory. We use computational tools and the hydrodynamic formulation of the Gross–Pitaevskii equation, coupled with the Poisson equation, to investigate the effect of this potential on the core–tail structure and the behavior of the resulting rotation curves. Our analysis is, in principle, qualitative, but also quantitative for specific cases, focusing on the influence of model parameters on halo morphology and solutions to the associated dynamic system.

We show that the core–tail model satisfactorily reproduces the profile presented in several galaxies, achieving competitive performance in relation to classical empirical profiles, such as NFW, Einasto, and Burkert, always adopting the minimum disk approach. We know that a fully realistic description of galactic rotation curves requires the inclusion of baryonic components such as the stellar disk, bulge, and gas. Including these contributions would likely modify the best-fit values of the dark matter parameters. However, we expect this effect to be primarily quantitative, rather than qualitative, as the main structural features of the rotation curves can already be reproduced within the adopted approximation. A full baryon + dark matter decomposition will be explored in future work. We saw that the Kapitza potential plays a relevant role by introducing an additional mechanism capable of sensitively modulating the shape of the tail, influencing the radial decay of density and the scale of orbital velocities.

The model still involves questions that require further investigation. Among them, we highlight the need to understand the origin and physical interpretation of the Kapitza potential in astrophysical contexts, as well as to analyze the stability of the oscillations induced in the tail density. Future studies that systematically explore the parameter space and perform direct comparisons with fully numerical simulations may clarify these limitations and better delineate the regime of applicability of the model. Within these limitations, however, the results obtained here indicate that the introduction of the Kapitza potential significantly expands the set of possible solutions in Bose–Einstein condensate models for dark matter, providing a promising alternative for describing galactic halos with a core–tail structure.

Author Contributions: Conceptualization, I.B.; Methodology, I.B.; Validation, H.V.; Formal analysis, H.V.; Investigation, H.V.; Resources, H.V.; Data curation, I.B.; Writing—original draft, H.V.; Writing—review & editing, I.B. and H.V.; Project administration, H.V.; Funding acquisition, H.V. All authors have read and agreed to the published version of the manuscript.

Funding: This work was supported by the Research Support Foundation of the State of Minas Gerais (FAPEMIG), the Research Support Foundation of the State of Espírito Santo (FAPES), and the Brazilian federal agencies CNPq and CAPES.

Data Availability Statement: The raw data supporting the conclusions of this article will be made available by the authors on request.

Acknowledgments: The authors thank Iván Álvarez for helpful comments and clarifications and acknowledge the use of the computational resources provided by the SciCom Lab of the Department of Physics at UFES.

Conflicts of Interest: The authors declare no conflicts of interest.

References

1. Zwicky, F. Die Rotverschiebung von extragalaktischen Nebeln. *Helv. Phys. Acta* **1933**, *6*, 110–127.
2. Rubin, V.C.; Ford, W.K., Jr. Rotation of the Andromeda Nebula from a Spectroscopic Survey of Emission Regions. *Astrophys. J.* **1970**, *159*, 379. [CrossRef]
3. Cirelli, M.; Strumia, A.; Zupan, J. Dark Matter. *arXiv* **2024**, arXiv:2406.01705. [CrossRef]
4. Bertone, G.; Hooper, D.; Silk, J. Particle dark matter: Evidence, candidates and constraints. *Phys. Rep.* **2005**, *405*, 279–390. [CrossRef]
5. Bertone, G.; Hooper, D. History of dark matter. *Rev. Mod. Phys.* **2018**, *90*, 045002. [CrossRef]
6. Feng, J.L. Dark matter candidates from particle physics and methods of detection. *Annu. Rev. Astron. Astrophys.* **2010**, *48*, 495–545. [CrossRef]
7. Navarro, J.F.; Frenk, C.S.; White, S.D.M. A Universal Density Profile from Hierarchical Clustering. *Astrophys. J.* **1997**, *490*, 493–508. [CrossRef]
8. Einasto, J. On the Construction of a Composite Model for the Galaxy and on the Determination of the System of Galactic Parameters. *Tr. Astrofiz. Instituta Alma-Ata* **1965**, *5*, 87–100.
9. Burkert, A. The Structure of Dark Matter Halos in Dwarf Galaxies. *Astrophys. J. Lett.* **1995**, *447*, L25–L28. [CrossRef]
10. de Blok, W.J.G. The Core-Cusp Problem. *Adv. Astron.* **2009**, *2010*, 789293. [CrossRef]
11. Del Popolo, A.; Le Delliou, M. Small Scale Problems of the ΛCDM Model: A Short Review. *Galaxies* **2017**, *5*, 17. [CrossRef]
12. Weinberg, D.H.; Bullock, J.S.; Governato, F.; de Naray, R.K.; Peter, A.H.G. Cold dark matter: Controversies on small scales. *Proc. Natl. Acad. Sci. USA* **2015**, *112*, 12249–12255. [CrossRef]
13. de Blok, W.J.G.; Walter, F.; Brinks, E.; Trachternach, C.; Oh, S.H.; Kennicutt, R.C., Jr. High-Resolution Rotation Curves and Galaxy Mass Models from THINGS. *Astron. J.* **2008**, *136*, 2648–2719. [CrossRef]
14. Marsh, D.J. Axion cosmology. *Phys. Rep.* **2016**, *643*, 1–79. [CrossRef]
15. Berezhiani, Z.G.; Khlopov, M.Y. Cosmology of spontaneously broken gauge family symmetry with axion solution of strong CP-problem. *Z. Für Phys. C Part. Fields* **1991**, *49*, 73–78. [CrossRef]
16. Khlopov, M.Y.; Malomed, B.A.; Zeldovich, I.B.; Zeldovich, Y.B. Gravitational instability of scalar fields and formation of primordial black holes. *Mon. Not. Roy. Astron. Soc.* **1985**, *215*, 575–589. [CrossRef]
17. Böhmer, C.G.; Harko, T. Can dark matter be a Bose–Einstein condensate? *J. Cosmol. Astropart. Phys.* **2007**, *2007*, 025. [CrossRef]
18. Schive, H.Y.; Liao, M.H.; Woo, T.P.; Wong, S.K.; Chiueh, T.; Broadhurst, T.; Hwang, W.Y.P. Understanding the Core-Halo Relation of Quantum Wave Dark Matter from 3D Simulations. *Phys. Rev. Lett.* **2014**, *113*, 261302. [CrossRef] [PubMed]
19. Hui, L.; Ostriker, J.P.; Tremaine, S.; Witten, E. Ultralight scalars as cosmological dark matter. *Phys. Rev. D* **2017**, *95*, 043541. [CrossRef]
20. Hu, W.; Barkana, R.; Gruzinov, A. Cold and fuzzy dark matter. *Phys. Rev. Lett.* **2000**, *85*, 1158–1161. [CrossRef]
21. Bose, S.N. Plancks gesetz und lichtquantenhypothese. *Z. Für Phys.* **1924**, *26*, 178–181. [CrossRef]
22. Einstein, A. Quantentheorie des einatomigen idealen gases (zweite abhandlung). In *Akademie-Vorträge: Sitzungsberichte der Preußischen Akademie der Wissenschaften*; Wiley: Hoboken, NJ, USA, 1925; pp. 245–257.
23. Griffin, A.; Snoke, D.W.; Stringari, S. *Bose-Einstein Condensation*; Cambridge University Press: Cambridge, UK, 1996.
24. Gross, E.P. Structure of a quantized vortex in boson systems. *Il Nuovo Cimento (1955–1965)* **1961**, *20*, 454–477. [CrossRef]
25. Pitaevskii, L.P. Vortex lines in an imperfect Bose gas. *Sov. Phys. JETP* **1961**, *13*, 451–454.
26. Anderson, M.H.; Ensher, J.R.; Matthews, M.R.; Wieman, C.E.; Cornell, E.A. Observation of Bose-Einstein condensation in a dilute atomic vapor. *Science* **1995**, *269*, 198–201. [CrossRef]
27. Ketterle, W.; Durfee, D.S.; Stamper-Kurn, D. Making, probing and understanding Bose-Einstein condensates. *arXiv* **1999**. [CrossRef]
28. Chavanis, P.H. Self-gravitating Bose-Einstein Condensates. In *Quantum Aspects of Black Holes*; Calmet, X., Ed.; Springer International Publishing: Cham, Switzerland, 2015; pp. 151–194. [CrossRef]
29. Chavanis, P.H. Predictive model of BEC dark matter halos with a solitonic core and an isothermal atmosphere. *Phys. Rev. D* **2019**, *100*, 083022. [CrossRef]
30. Schive, H.Y.; Chiueh, T.; Broadhurst, T. Cosmic structure as the quantum interference of a coherent dark wave. *Nat. Phys.* **2014**, *10*, 496–499. [CrossRef]
31. Álvarez-Rios, I.; Guzmán, F.S. Spherical solutions of the Schrödinger-Poisson system with core-tail structure. *Phys. Rev. D* **2023**, *108*, 063519. [CrossRef]
32. Kapitza, P.L. Dynamic stability of the pendulum with vibrating suspension point. *Sov. Phys. JETP* **1951**, *21*, 588–597.
33. He, W.; Liu, C.Y. Oscillatory states of quantum Kapitza pendulum. *Ann. Phys.* **2023**, *449*, 169218. [CrossRef]
34. Jiang, J.; Bernhart, E.; Röhrle, M.; Benary, J.; Beck, M.; Baals, C.; Ott, H. Kapitza Trap for Ultracold Atoms. *Phys. Rev. Lett.* **2023**, *131*, 033401. [CrossRef]
35. Lelli, F.; McGaugh, S.S.; Schombert, J.M. SPARC: Mass models for 175 disk galaxies with spitzer photometry and accurate rotation curves. *Astron. J.* **2016**, *152*, 157. [CrossRef]
36. Rosen, G. Particlelike Solutions to Nonlinear Complex Scalar Field Theories with Positive-Definite Energy Densities. *J. Math. Phys.* **1968**, *9*, 996–998. [CrossRef]

37. Bialynicki-Birula, I.; Mycielski, J. Nonlinear Wave Mechanics. *Ann. Phys.* **1976**, *100*, 62–93. [CrossRef]
38. Haghani, Z.; Harko, T. Bose-Einstein condensate dark matter with logarithmic nonlinearity. *Phys. Rev. D* **2026**, *113*, 044005. [CrossRef]
39. Zloshchastiev, K.G. Sound Propagation in Cigar-Shaped Bose Liquids in the Thomas-Fermi Approximation: A Comparative Study between Gross-Pitaevskii and Logarithmic Models. *Fluids* **2022**, *7*, 358. [CrossRef]
40. Zloshchastiev, K.G. Resolving the puzzle of sound propagation in a dilute Bose–Einstein condensate. *Int. J. Mod. Phys. B* **2022**, *36*, 2250121. [CrossRef]
41. Madelung, E. Quantentheorie in hydrodynamischer Form. *Z. Für Phys.* **1927**, *40*, 322–326. [CrossRef]
42. Bohm, D. A Suggested Interpretation of the Quantum Theory in Terms of "Hidden" Variables. I. *Phys. Rev.* **1952**, *85*, 166–179. [CrossRef]
43. Merritt, D.; Graham, A.W.; Moore, B.; Diemand, J.; Terzić, B. Empirical Models for Dark Matter Halos. I. Nonparametric Construction of Density Profiles and Comparison with Parametric Models. *Astron. J.* **2006**, *132*, 2685. [CrossRef]
44. Retana-Montenegro, E.; Van Hese, E.; Gentile, G.; Baes, M.; Frutos-Alfaro, F. Analytical properties of Einasto dark matter haloes. *Astron. Astrophys.* **2012**, *540*, A70. [CrossRef]
45. Mocz, P.; Vogelsberger, M.; Robles, V.H.; Zavala, J.; Boylan-Kolchin, M.; Fialkov, A.; Hernquist, L. Galaxy formation with BECDM—I. Turbulence and relaxation of idealized haloes. *Mon. Not. R. Astron. Soc.* **2017**, *471*, 4559–4570. [CrossRef]
46. Virtanen, P.; Gommers, R.; Oliphant, T.E.; Haberland, M.; Reddy, T.; Cournapeau, D.; Burovski, E.; Peterson, P.; Weckesser, W.; Bright, J.; et al. SciPy 1.0: Fundamental algorithms for scientific computing in Python. *Nat. Methods* **2020**, *17*, 261–272. [CrossRef] [PubMed]
47. Bevington, P.R.; Robinson, D.K. *Data Reduction and Error Analysis for the Physical Sciences*; McGraw-Hill Education: Columbus, OH, USA, 2003.
48. Helou, G.; Madore, B.F.; Schmitz, M.; Bicay, M.D.; Wu, X.; Bennett, J. The NASA/IPAC extragalactic database. In *Proceedings of the Databases and On-Line Data in Astronomy*; Albrecht, M.A., Egret, D., Eds.; Astrophysics and Space Science Library; Springer: Dordrecht, The Netherlands, 1991; Volume 171, pp. 89–106. [CrossRef]
49. Yavetz, T.D.; Li, X.; Hui, L. Construction of wave dark matter halos: Numerical algorithm and analytical constraints. *Phys. Rev. D* **2022**, *105*, 023512. [CrossRef]

Disclaimer/Publisher's Note: The statements, opinions and data contained in all publications are solely those of the individual author(s) and contributor(s) and not of MDPI and/or the editor(s). MDPI and/or the editor(s) disclaim responsibility for any injury to people or property resulting from any ideas, methods, instructions or products referred to in the content.